

Characteristics of counter-rotating vortex rings formed ahead of a compressible vortex ring

Murugan Thangadurai · Debopam Das

Received: 19 August 2008/Revised: 15 March 2010/Accepted: 19 March 2010/Published online: 8 April 2010
© Springer-Verlag 2010

Abstract Characteristics of high Mach number compressible vortex ring generated at the open end of a short driver section shock tube is studied experimentally using high-speed laser sheet-based flow visualization. The formation mechanism and the evolution of counter rotating vortex ring (CRVR) formed ahead of the primary vortex ring are studied in details for shock Mach number (M) 1.7, with different driver section lengths. It has been observed that the strength of the embedded shock, which appears at high M , increases with time due to the flow expansion in the generating jet. Strength of the embedded shock also varies with radius; it is strong at smaller radii and weak at larger radii; hence, it creates a velocity gradient ahead of the embedded shock. At critical Mach number ($M_c \geq 1.6$), this shear layer rolls up and forms a counter rotating vortex ring due to Biot-Savart induction of the vortex sheet. For larger driver section lengths, the embedded shock and the resultant shear layer persists for a longer time, resulting in the formation of multiple CRVRs due to Kelvin–Helmholtz type instability of the vortex sheet. CRVRs roll over the periphery of the primary vortex ring; they move upstream due to their self-induced velocity and induced velocity imparted by primary ring, and interact with the trailing jet. Formation of these vortices depends strongly upon the embedded shock strength and the length of the generating

jet. Primary ring diameter increases rapidly during the formation and the evolution of CRVR due to induced velocity imparted on the primary ring by CRVR. Induced velocity of CRVR also affects the translational velocity of the primary ring considerably.

List of symbols

M	Incident shock Mach number inside the shock tube
M_c	Critical Mach number at which counter rotating vortices form
U_b	Velocity behind the incident shock at shock tube exit
a	Local speed of sound
u, v	Axial and radial velocity components
ℓ	Driver section length of the shock tube
D	Inner diameter of the shock tube
V_r	Translational velocity of the vortex ring
V_s	Shock speed inside the tube
D_r	Diameter of the vortex ring
t	Time, where $t = 0$ represents incident shock at tube exit
$t^* = tU_b/D$	Non-dimensional time
CRVR	Counter rotating vortex ring
U_i	Induced velocity of CRVR

M. Thangadurai (✉)
Central Mechanical Engineering Research Institute (CMERI),
Durgapur, West Bengal, India
e-mail: Murugan.thangadurai@gmail.com

D. Das
Department of Aerospace Engineering, IIT Kanpur,
Kanpur, Uttar Pradesh 208016, India
e-mail: das@iitk.ac.in

1 Introduction

Study of compressible vortex ring generated at the open end of a shock tube at high incident shock Mach number (M) is important due to the presence of shock and expansion waves in the flow field and large variations in the thermodynamic and the physical properties across the

vortex ring. Though the generation-mechanism is simple, the unsteady nature of the flow field facilitates understanding many transient flows and supersonic turbulence. There are very few experimental studies available for compressible vortex ring at high M . Compressible vortex ring emerging from an open end of a shock tube was first observed experimentally by Elder and Hass (1952). They calculated the trajectory of the vortex ring and the incident shock, using spark Schlieren photographs for $M = 1.12$ & 1.32 . Moore (1985) found theoretically that the propagation velocity of subsonic vortex rings is less if the flow is considered compressible and is comparatively more if the flow is considered incompressible. Arakeri et al. (2004) studied the flow field of a vortex ring at the open end of a short driver section shock tube, using Particle Image Velocimetry (PIV). They examined the early evolution of the vortex ring for three different $M = 1.1, 1.2$ & 1.3 . They observed that the translational velocity of the ring after formation is $0.7U_b$, where U_b is the velocity behind the shock at shock tube exit which is calculated from moving normal shock relations, using measured shock Mach number. However, velocity at the exit initially increases as flow expands and reduces gradually as the expansion waves from the driver section reaches the shock tube exit.

Flow velocity, density, temperature and pressure behind the incident shock increase as M increases (shock tube relations, Anderson 1982). This causes more expansion of flow at the exit during vortex ring formation, and complicated expansion/shock wave-structures are observed at high M . Phan and Stollery (1983) first noted the presence of embedded shock (see Figs. 2f–g, 3) in the axial region (Fig. 2h) of a vortex ring, besides expansion waves at the exit, using schlieren photographs for $M = 1.5$. They confirmed the presence of an embedded shock and its rearward facing nature (along the axial direction, the embedded shock profile is straight and is curved inwards near the vortex core as seen in Figs. 2h, 3) through pressure measurements along the axis. Baird (1987) verified more clearly the shock structure formed during the evolution of vortex ring, using differential interferometry. He calculated velocity, pressure and temperature at different regions using on-axis pressure measurements and verified the measured quantities with steady, quasi-1-D shock/expansion wave relations. He noted that the De-Laval nozzle type flow experienced at the axial region due to the presence of vortex ring is responsible for the embedded shock formation. He also found that the rearward facing embedded shock does not extend up to the vortex core and disappears in the region where viscous effects dominate.

Brouillette et al. (1995) found that the threshold Mach number for embedded shock formation is 1.34 when the driver section length is larger than the critical length. Critical length is defined as a driver section length at which

the first expansion waves reflected from the rear end of the shock tube catches the incident shock at the shock tube exit. Brouillette and Hebert (1997) observed the appearance of embedded shock at $M = 1.43$ using critical length. They also observed a phenomenon of counter rotating vortex ring (CRVR) formation ahead of the main vortex ring for critical Mach number ($M_c \geq 1.6$) using shadow-graph technique. They stated that the embedded shock forms due to supersonic flow in the axial region of the vortex ring, and the CRVR forms due to flow separation caused by the adverse pressure gradient across the embedded shock. They also mentioned that the CRVR merges with the primary ring because of mutual interaction during its evolution and becomes poorly defined vortical structure at later stage. However, it is unclear what Brouillette and Hebert (1997) mean by flow separation across the shock. Minota (1998) also observed the formation of CRVR and embedded shock in the axial region of the impulsive flow generated from the shock tube while studying the interaction of vortex ring and shock wave.

Kontis et al. (2006) observed the formation of multiple CRVR ahead of the primary vortex ring for $M = 1.63$ using high-speed schlieren photography during their study of vortex ring interaction with generic bodies. They studied the flow field of compressible vortex ring for three Mach numbers 1.28, 1.52 and 1.63 using a shock tube with the driver and the driven section length of 750 and 1310.5 mm, respectively. They found that for $M = 1.28$, the vortex ring generated at shock tube exit is shock free, whereas for $M = 1.48$, an embedded shock is formed in the axial region and for $M = 1.63$ multiple CRVRs are formed ahead of primary vortex ring, besides the formation of strong-embedded shock. They stated that a larger number of tiny CRVRs will be generated as the compressibility increases (M increases). Study of head-on collision of a vortex ring with the solid and perforated walls by Kontis et al. (2008) using high-speed schlieren technique also exhibits formation of multiple CRVRs.

The present paper focuses on the mechanism of CRVR formation, its subsequent evolution with space and time along with the effects of CRVR on translational velocity and diameter of the primary vortex ring. Flow has been generated at the open end of a shock tube. Effects of Mach numbers and driver section lengths have been addressed. It has been observed that CRVR rolls over the periphery of a primary vortex ring interact with the trailing jet after reaching the rear side of the primary vortex ring. In this paper, the term generating jet implies the jet attached to the leading vortex ring and the term trailing jet means the detached jet that is no longer involved in the formation of vortex ring. The observed evolution of CRVR is entirely different from the evolution stated by Brouillette and Hebert (1997) where CRVR merges with the primary ring

after its formation. Murugan and Das (2007b) studied the evolution of CRVR along with its acoustic characteristics for $M = 1.69$. They found that the acoustic fluctuations generated during embedded shock-vortex ring interaction and the formation of CRVR is dominant compared to the roll up and formation of primary ring. Murugan and Das (2009) has also shown the complete evolution of single CRVR formed ahead of the primary vortex ring for $M = 1.7$ using high-speed smoke visualizations.

For impulsive under-expanded flow emerging from the open end of a shock tube, the shock and expansion wave structures are shown by Baird (1987); Brouillette and Hebert (1997); Minota (1998) and Kontis et al. (2006, 2008). However, these visualization pictures have not shown the details of the flow field because of the integral nature of the visualization techniques (interferometry, schlieren and shadowgraph) that respond to the density variations. Shadowgraph, Schlieren and interferometry images are two-dimensional projections of a three-dimensional density field. Hence, all depth information along the optical axis is lost. Other studies of compressible vortex ring (Arakeri et al. 2004; Aure and Jacobs 2008; Haertig et al. 2006, Cetegen and Hermanson 1995) are for low M . Though Brouillette and Hebert (1997) and Kontis et al. (2006, 2008) observed the CRVR ahead of the main vortex ring, neither the mechanism of CRVR formation nor its evolution are discussed because of the limitations of the visualization techniques used.

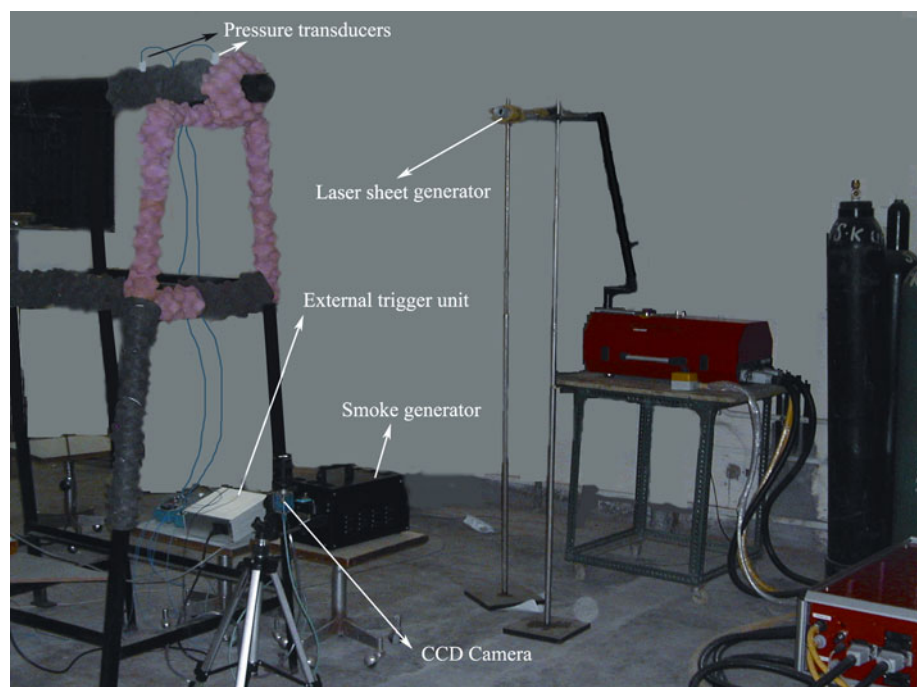
Unlike schlieren and interferometry techniques, flow field is illuminated using smoke particles and laser light sheet in the present experiments. As the flow is axisymmetric, here it is visualized in a horizontal diametrical

plane rather than exposing the entire flow field like in optical techniques. Strong-embedded shock is observed in few flow visualization pictures where the smoke intensity is optimum. Though earlier studies (Baird 1987; Brouillette and Hebert 1997, Kontis et al. 2008) show the formation of embedded shock in the axial region using optical techniques, the same is identified here from variation in leading smoke front during evolution of the vortex ring at different times. As the fluid inside the shock tube rolls over the ambient fluid during formation, the vortex ring's core is always filled with ambient fluid (no smoke particles) for laminar vortex ring. However, the vortex ring's core is filled with smoke as the ring becomes turbulent due to velocity fluctuations. Effect of the driver section length (ℓ) and the Mach number (M) on the CRVR formation is presented. The variation in the diameter of vortex ring at different M and ℓ is also presented along with the mechanism responsible for the diameter variations.

2 Experimental setup

A cylindrical shock tube (as shown in Fig. 1) of variable driver section length is used for generating compressible vortex ring. Inner and outer diameters of the shock tube are 64 and 100 mm, respectively. Maximum driver section length is 315 mm and the driven section length is 1,200 mm. The exit of the shock tube is made sharp with 60° chamfers. Length of the driver section is varied by placing cylindrical aluminum blocks of various lengths inside the tube. The shock tube is kept at a height of 1.78 m

Fig. 1 Experimental setup



to avoid any interaction between the flow and the reflected shock from the floor. At the highest Mach number ($M < 2.1$) considered here, the incident shock reflects back to the flow from the ground only after few milliseconds (>6 ms). The entire evolution of CRVR occurs at less than $2,500 \mu\text{s}$ and hence, the flow field is free from reflected shocks. Signals from pressure transducers kept inside the shock tube are measured using NI 4472, 24-bit card with 100 kHz sampling rate. To achieve high M , helium is used as a driver section gas for all experiments. Mylar sheets of different thickness are used as diaphragms that are ruptured using a heated nichrome wire.

The shock speed (V_s) is measured from the difference in arrival time of the shock at two pressure transducers kept 300 mm apart inside the shock tube. The first transducer is kept at a distance of 200 mm from exit. Shock Mach number (M) is calculated from the shock speed and ambient speed of sound. Mach number can vary slightly in different experiments due to improper bursting of diaphragms,

uneven heating of diaphragms and slight changes in driver section pressure. Maximum variations of M in repeated experiments are found to be within $\pm 1.8\%$. The shock tube driven section is filled with a desired amount of paraffin oil smoke for flow visualization. The ambient fluid outside the shock tube is not seeded with smoke particles. However, small amount of smoke is usually present near the shock tube exit after seeding. These smoke particles do not affect the flow field of vortex ring (Fig. 2g, h) due to their negligible velocity. Hence, the illuminated flow field is essentially the fluid that comes out from the driven section of the shock tube. The flow field is captured using a double-pulsed Nd: YAG laser (Quanta system, 200 mJ/pulse) and a CCD camera (Pixelfly 1,280 \times 1,024 pixels). The laser and the CCD camera are synchronized using an external synchronizing unit, which receives trigger signal from the pressure transducer kept inside the shock tube. The flow fields at different times are obtained by varying the delay in the synchronizing unit, which can be varied from 1 μs to 10 ms.

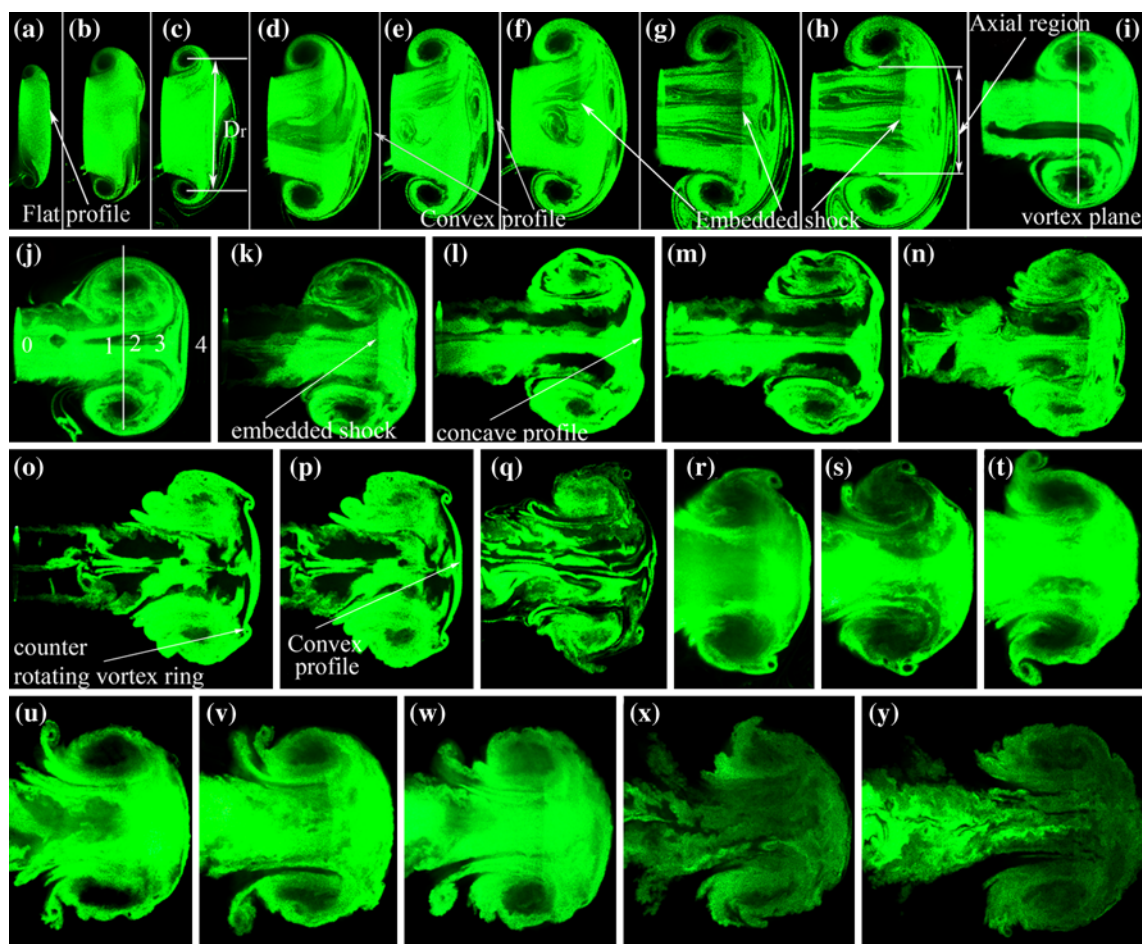


Fig. 2 Formation and evolution of CRVR for $M = 1.7$ and $\ell = 165$ mm at different times, $t =$ (a) 34 μs (b) 67 μs (c) 104 μs (d) 164 μs (e) 184 μs (f) 224 μs (g) 277 μs (h) 317 μs (i) 504 μs (j)

574 μs (k) 674 μs (l) 744 μs (m) 784 μs (n) 847 μs (o) 954 μs (p) 994 μs (q) 1,064 μs (r) 1,074 μs (s) 1,167 μs (t) 1,280 μs (u) 1,367 μs (v) 1,480 μs (w) 1,607 μs (x) 1,767 μs (y) 1,967 μs

3 Results and discussion

Results are presented in following sequence. Initial stage of evolution along with the characteristics of under-expanded flow behind the ring is discussed first. Subsequently, the mechanism of CRVR formation, the growth and motion of CRVR, and their interaction with each other and trailing jet are discussed. The vortex ring diameter is defined as the distance between the centers of the cores in cross-sectional view of the vortex ring (Fig. 2c). The ring diameters at different time are measured from flow visualization pictures. Translational velocity (V_T) of the primary vortex ring is measured from the displacement of the vortex core in two consecutive images obtained at 30 μs time difference. The time difference between two consecutive images is kept large enough to have sufficient pixel displacement of vortex core. Viewing area of the camera is varied according to the size of the vortex ring, to improve the accuracy of measurement. For example, during early stage of formation, the ring size is small ($\approx D$) hence small area is focused. Minimum pixel displacement of the vortex centers in horizontal direction for $M = 1.7$ between two consecutive images at $t = 42 \mu\text{s}$ and $t = 72 \mu\text{s}$ is 15 pixels. Corresponding pixel displacement in radial direction is 26 pixels. Axial (u) and lateral (v) components of velocity of CRVR are also measured from flow visualization pictures. The outward velocity of CRVR is taken as positive and the inward velocity as negative. Though the vortex core is laminar and circular during its formation (Fig. 2a–e), soon it becomes turbulent and non-circular (Fig. 2n–t) as observed during its evolution in the cross-sectional view, where the centers of the vortex cores are identified approximately visually. Hence, the translational velocity of CRVR, measured during its evolution may have $\pm 10\%$ variation.

3.1 Flow expansion at the open end and formation of vortex ring

Formation and growth of the primary vortex ring for $M = 1.7$ and $\ell = 165 \text{ mm}$ is shown in Fig. 2. Figure 2a–h shows details of the early stage of evolution, while Fig. 2i–t shows the later stage when CRVR forms. The incident shock diffracts at exit and the fluid behind it expands due to strong favorable pressure gradient between the ambient and the shock tube fluid. Flow visualization pictures in Fig. 2a–c, ($t \approx 34\text{--}104 \mu\text{s}$) show the roll up of the vortex sheet that occurs to satisfy the Kutta condition (Saffman 1978) at sharp exit after diffraction of the incident shock. The core of the vortex ring is stable and laminar during the rolling up process. The diameter of the vortex ring increases rapidly during initial roll up (Fig. 2a–e, up to $t = 184 \mu\text{s}$) and rapid expansion of flow in the generating jet aids to the growth.

The rate of expansion is more for large M cases compared to small M flow (Murugan 2008). The vortex ring moves predominantly downstream after initial formation (Fig. 2f–j).

Vortex sheet in the generating jet behind the primary vortex ring (Fig. 2g) forms tiny shear layer vortices due to Kelvin–Helmholtz type instability. Glezer (1988) observed transition of vortex ring from laminar to turbulent state in water tunnel using piston cylinder arrangement. He found that the Kelvin–Helmholtz-like instability developed at the vortex sheet at high Reynolds numbers, initiates the transition process. He also found that the vortex ring becomes turbulent quickly after formation at sufficiently large Reynolds number. Lim (1997) proposed a model for incompressible turbulent ring, where the leapfrogging and the tilting of secondary vortex ring formed at the generating jet is responsible for turbulent ring formation in addition to Kelvin–Helmholtz-like instability. The shear layer vortices of the generating jet propagate into the vortex core in Fig. 2d–g and cause instability of the vortex core in Fig. 2h–k. The unstable core of the vortex ring eventually becomes turbulent in Fig. 2n–q. This phenomenon is also identified by Murugan and Das (2008) for comparatively less M ($M = 1.55$) using high-speed flow visualizations.

Reynolds number of the flow behind the incident shock for $M = 1.7$ is 3.372×10^6 as compared to 2.313×10^6 for $M = 1.55$. Thus, the density difference between the jet and ambient and Reynolds number is higher for $M = 1.7$ compared to $M = 1.55$, resulting rapid transition by increasing the growth of instabilities. When the transition process is rapid, the vortex ring's core becomes non-circular (Fig. 2l) and turbulent (Fig. 2q) before pinching-off. The pinching-off (Gharib et al. 1998) of the leading vortex ring occurs when vortex ring's vorticity field separates from the generating jet's shear layer owing to its self-induced velocity. It is difficult to identify the exact pinching-off time from the flow visualizations. Emergence of the jet that is not entrained into primary ring is considered as an indicator for pinching-off initiation. Reduced jet diameter in the axial region of vortex ring in Fig. 2y at $t = 1,967 \mu\text{s}$ compared to Fig. 2v–w indicates the initiation of isolation process of the vortex ring from the jet. The initiation of pinching-off can also be observed in Fig. 5p–q. Pinching-off process occurs over certain time duration and a precise knowledge of it can be obtained from Gharib et al. 1998 for incompressible flow. It cannot be obtained only through flow visualization and is not considered in this paper.

The leading flat smoke front along the axial region, at $t = 34 \mu\text{s}$ in Fig. 2a shows the initiation of flow expansion, after diffraction of the incident shock during which the vortex sheet rolls up. This flat smoke front is due to uniform flow behind the shock at the exit. It gradually becomes convex as the flow expands supersonically at the

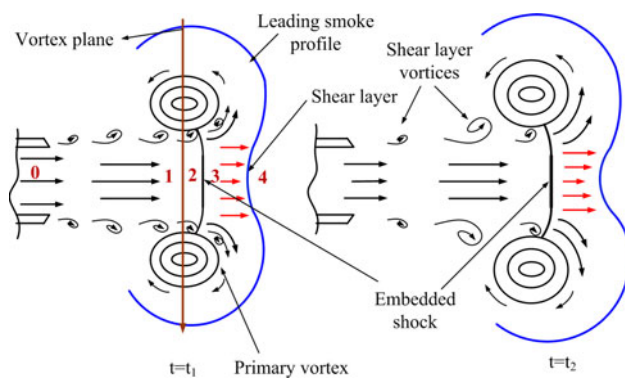


Fig. 3 Schematic diagram shows the flow field of generating jet at time $t = t_1$ and t_2 for $M = 1.7$

exit during vortex ring's growth in Fig. 2b–d. The shock/expansion waves formed in the flow field during expansion of the flow from the shock tube is reported in literature for $M = 1.5$ (Phan and Stollery 1983; Baird 1987) and $M = 1.63$ (Kontis et al. 2006, 2008). Baird (1987) calculated thermodynamic quantities, pressure, temperature, density, flow velocity, and M at different sections (0, 1, 2, and 3 in Figs. 2j, 3) using the visualized oblique shock wave angles and pressure measurements at different sections for $M = 1.5$. In Baird's (1987) case, the pressure, $2.48 \times 10^5 \text{ N/m}^2$ and the velocity, 236 m/s behind the incident shock at the exit produce pressure, $0.8 \times 10^5 \text{ N/m}^2$ and velocity, 518 m/s in the region 0 (Fig. 2j) due to flow expansion. As in the present study, flow is visualized by illuminating particles the wave angles are not visible. Hence, the above analysis of Baird (1987) is not performed. However, flow properties behind the incident shock at exit are calculated using measured $M = 1.7$ inside the shock tube and the moving normal shock relations (Anderson 1982). The static pressure and the velocity behind the shock at exit are $3.18 \times 10^5 \text{ N/m}^2$ and 317.37 m/s, respectively. As the pressure and the velocity behind the shock at the exit for $M = 1.7$ are much higher than the Baird's (1987) case ($M = 1.5$), the generating jet velocity at region 0 in Fig. 2j is larger than 518 m/s (velocity measured by Baird 1987 for $M = 1.5$). From Fig. 2a–j, it is observed that flow evolves from purely divergent flow (Fig. 2d dotted line) to converging–diverging (Fig. 2j dotted line) nozzle type flow as observed by Baird (1987).

For $M < 1.5$, the expansion waves reflected from the driver section wall catches the incident shock much earlier compared to the high M cases. As the leading expansion wave travels toward the rear end of the shock tube with the slope of $1/a$ ($a =$ speed of sound) irrespective of M in the x – t diagram (Anderson 1982), it first catches the incident shock, which travels slow. Thus, the flow is not clean for these cases. This results in expansion of flow for short

duration for low M , which in turn produces either supersonic flow for short duration or subsonic flow in the generating jet. Hence, the primary vortex ring is not affected rigorously by the generating jet for low M and moves like a laminar vortex ring downstream (Murugan and Das 2007a). The translational velocity of the ring measured at $t = 534 \mu\text{s}$ is 225 m/s. The asymptotic translational velocity of the compressible vortex ring after pinching-off is approximately $0.7 U_b$ (Arakeri et al. 2004).

Formation of the embedded shock is observed at $t = 164 \mu\text{s}$ in Fig. 2f, where it is very weak. The embedded shock strength increases gradually from Fig. 2g–h. This is observed from the change in smoke intensity across the shock. The smoke particle ahead of the embedded shock in region 3 in Fig. 2h is brighter than that in region 2 due to increase in density across the embedded shock. Effect of the increase in strength of the embedded shock is also visible from change in leading smoke front. The convex smoke front in Fig. 2d–f gradually changes into straight profile in the axial region in Fig. 2j. This shows that the velocity in the axial region reduces gradually, possible only by increase in strength of the embedded shock. This embedded shock forms in the axial region ahead of vortex plane due to adverse pressure gradient resulting from over-expansion ahead of vortex plane. Presence of embedded shock in the axial region is observed clearly in Fig. 2g. The pressure and velocities (with reference to the vortex ring) measured by Baird (1987) across the embedded shock (at regions 2 and 3) are 74 ± 8 and 136 ± 9 kPa and 434 and 283 ± 8 m/s, respectively for $M = 1.5$. The large gradient in pressure and velocities from region 2 to region 3 and the interferometry visualizations confirmed the presence of embedded shock for $M = 1.5$. Baird (1987) proved from 1-D calculation that this embedded shock forms in the axial region due to C–D nozzle type flow experienced upstream and downstream of the vortex plane (Fig. 2i). Flow expansion at exit increases, as M increases resulting into the formation of strong embedded shock. Thus, it is inferred that the embedded shock also forms for $M = 1.7$, and its strength is more compared to that at $M = 1.5$.

3.2 Formation and evolution of CRVR

It is observed in the previous section that for high M flow, embedded shock forms (Fig. 2f–h, for $M = 1.7$, driver section length (ℓ) = 165 mm) due to C–D nozzle effect (Baird 1987). The embedded shock is normal along the axis of the vortex ring and curved near the vortex core (Fig. 2g–k); strength of the embedded shock gradually decreases with increasing radius. Nearly same intensity of smoke at regions 2 & 3 in Fig. 2r–w denotes disappearance of the embedded shock. Reduction in velocity ahead of the

shock at larger radii is less compared to that at smaller radii due to change in embedded shock strength in the radial direction (see Fig. 3). This induces a shear in the annulus fluid layer ahead of the embedded shock. This phenomenon is observed from flow visualization pictures in Fig. 2i–m, where the straight leading smoke front in the axial region becomes concave shaped as explained with a schematic in Fig. 3 at two different time instances, say t_1 and t_2 where $t_2 > t_1$.

Strength of the embedded shock increases with increase in M . As a consequence, the velocity gradient in the annulus shear layer becomes stronger than that at low M . At a critical Mach number ($M_c = 1.6$, for Brouillette and Hebert (1997) case), the flow velocity near the vortex core is much higher than the velocity near the axis of the ring (Fig. 2l). Hence, strong shear layer is formed ahead of the embedded shock, which is shown in Fig. 3, at $t = t_2$. Since the shear layer has a definite starting point (i.e., just ahead of the embedded shock), and it is a result of faster moving fluid at larger radii and slower moving fluid at smaller radii, it can be modeled as a semi-infinite shear layer as shown in Fig. 4a. By Biot-Savart induction, this vortex sheet rolls-up into spiral form as shown in Fig. 4b. The spiral roll-up process in relation to vortex ring formation has been simulated, modeled, and described in numerous studies (e.g., Pullin (1978, 1979), Nitsche and Krasny (1994)). The mechanism leading to the formation of primary vortex ring and first CRVR from the vortex sheets is the vortex sheet roll-up.

The circulation of the vortices formed ahead of the embedded shock is opposite to the primary vortex ring. Hence, it is termed as counter rotating vortex ring (Brouillette and Hebert 1997). CRVR, after formation, roll over the periphery of the primary vortex ring (Fig. 2n–v) upstream with respect to the primary ring due to their self-induced velocity and induced velocity imparted by the primary ring. In fact, the influence of the primary vortex ring on the CRVR's motion is expected to be dominant due to its larger circulation compared to that of CRVR. CRVR grows in size during their evolution. Nature of the induced

velocity of CRVR is discussed in detail at Sect. 3.7. CRVR after reaching the rear side of the primary ring ejects upstream (Fig. 2w). It interacts with the trailing jet (Fig. 2x–y) due to entrainment, and loses its identity quickly owing to its opposite circulation to the trailing jet vortices. The embedded shock begins to lose its strength during the growth and evolution of CRVR, due to reduction in trailing jet velocity (Fig. 2n). This can be seen in Fig. 2n–w where the concave leading smoke front in the axial region changes into convex profile. The convex profile forms when the velocity along the axis is higher than that along the shear region, possible only by reduction in the embedded shock strength. The embedded shock ultimately disappears far downstream in Fig. 2x as the trailing jet velocity becomes subsonic.

3.3 Formation and evolution of multiple CRVR

Multiple CRVR are observed as the driver section length (ℓ) increases from 165 mm to 315 mm for the same $M = 1.7$. Figure 5 shows the formation and evolution of multiple CRVRs. As ℓ increases, the embedded shock persists in the axial region for longer duration due to late arrival of expansion waves from the driver section to exit. Hence, the shear layer continues developing in the axial region. This leads to the formation of additional vortices behind the first CRVR due to Kelvin–Helmholtz type instability. The annulus shear layer is perturbed by fluctuations in turbulent vortex core and their interactions with the embedded shock. Andreopoulos et al. (2000) and Agui et al. (2005) found that the interaction between turbulent fluctuations and embedded shock is mutual during shock–turbulence interaction. The shock wave experiences substantial oscillations and deformation, and the characteristic velocity, timescales and length scales of turbulence changes considerably as a result of embedded shock–turbulent fluctuations interaction. They have also emphasized that the consequences of the interaction depends not only upon the strength, orientation, location, and shape of the shock wave but also upon the flow geometry, boundary conditions, state of turbulence, and compressibility of the incoming flow. The annulus layer of fluid with higher shear is also inviscidly unstable due to inflectional nature of velocity profile. Thus, the fluctuations in the shear layer rolls up into multiple CRVR as shown in Fig. 5f–h due to Kelvin–Helmholtz type instability (Lord Kelvin 1871). The shadowgraph images obtained by Zarebehtash et al. (2008) also shows the presence of CRVR ahead of embedded shock and stated that CRVRs are formed due to Kelvin–Helmholtz instability. Parameters, such as, embedded shock strength, its duration of presence in the generating jet, velocity and density variations in the shear layer, and the embedded shock–turbulence interactions, are responsible for subsequent nature of evolution of multiple CRVRs.

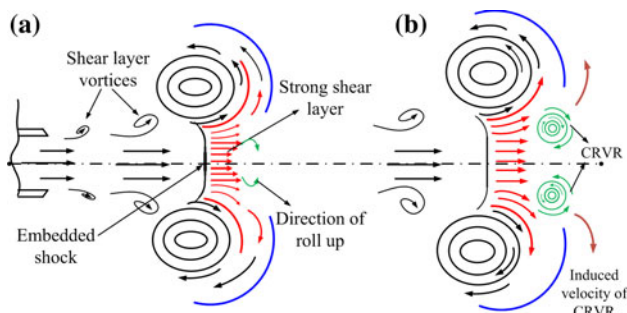


Fig. 4 Schematic showing roll up of the annulus vortex sheet into a vortex due to Biot-Savart interactions

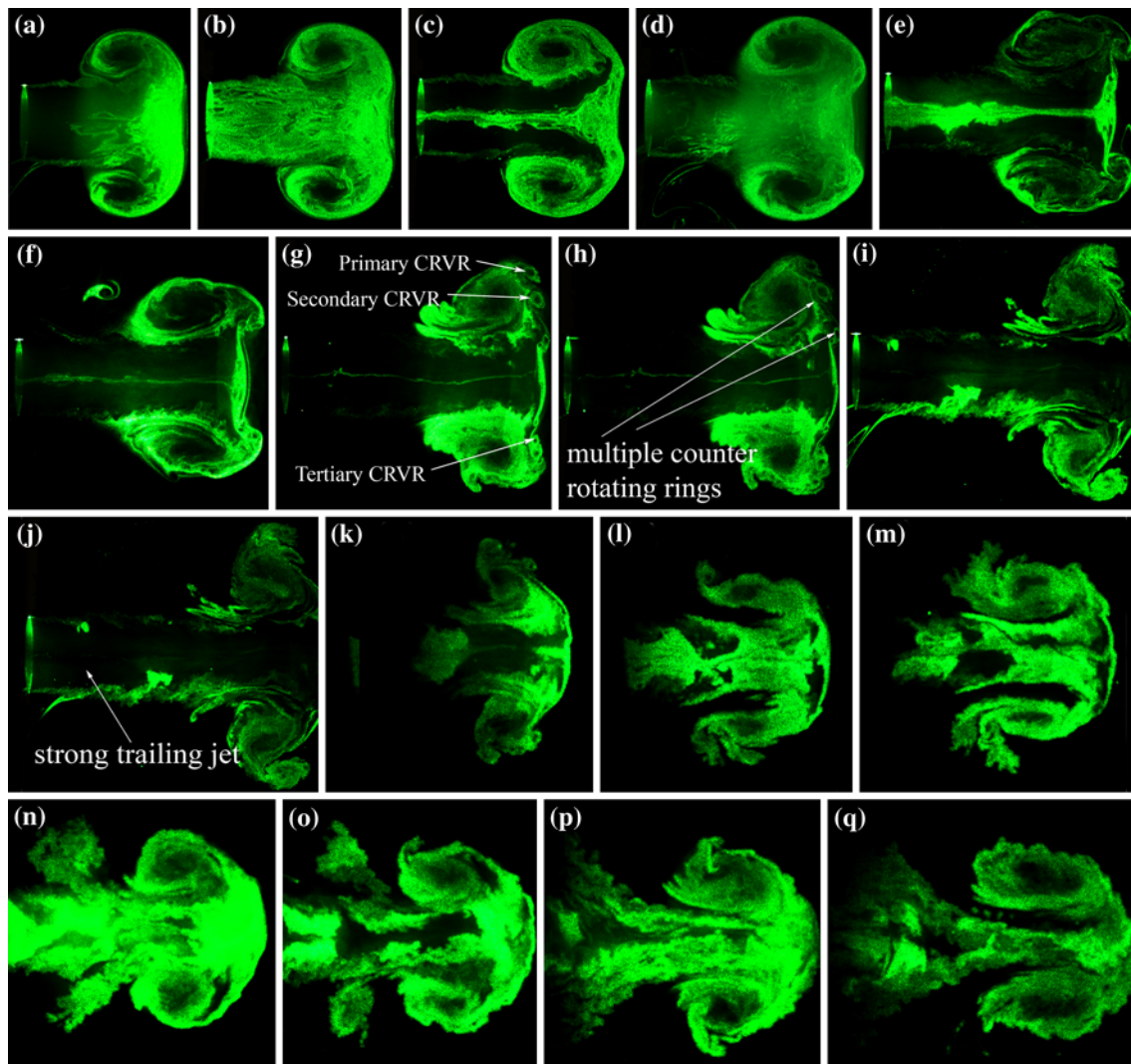


Fig. 5 Formation and evolution of multiple CRVR for $M = 1.7$, $\ell = 315$ mm at $t =$ (a) $445 \mu\text{s}$ (b) $507 \mu\text{s}$ (c) $580 \mu\text{s}$ (d) $673 \mu\text{s}$ (e) $803 \mu\text{s}$ (f) $863 \mu\text{s}$ (g) $1,003 \mu\text{s}$ (h) $1,043 \mu\text{s}$ (i) $1,083 \mu\text{s}$ (j) $1,213 \mu\text{s}$

(k) $1,153 \mu\text{s}$ (l) $1,373 \mu\text{s}$ (m) $1,480 \mu\text{s}$ (n) $1,680 \mu\text{s}$ (o) $1,780 \mu\text{s}$ (p) $2,040 \mu\text{s}$ (q) $2,146 \mu\text{s}$

Figure 5e shows the formation of first CRVR that is followed by secondary and tertiary CRVRs ahead of the primary ring as shown in Fig. 5f–g. Thus, multiple CRVRs are formed continuously ahead of the primary vortex ring (Fig. 5f–h) till the embedded shock loses its critical strength. The duration of flow expansion at the exit for two different ℓ is verified from clean flow time obtained analytically from inviscid flow calculations. Clean flow time is the time gap between the arrival of shock wave and the expansion waves at the tube exit. The durations of clean flow for $\ell = 165$ and 315 mm are 3.26 and $282 \mu\text{s}$, respectively. Hence, for $\ell = 315$ mm the flow expansion time is longer than that for $\ell = 165$ mm. Multiple CRVR are formed due to persistence of the embedded shock for a prolonged period.

These multiple CRVR move along the periphery of the primary ring either separately (with a tendency of merging, Fig. 5g) or merged together due to leap-frogging action (Fig. 5j). Multiple CRVRs' interaction makes the flow asymmetric with respect to axial direction (Fig. 5g). It is verified from several experiments that the asymmetry is present for $M = 1.7$ with $\ell = 315$ mm, whereas it doesn't exist for small M cases. The asymmetry is not observed also during the formation and the growth of the first CRVR (Figs. 2m–r, 5d–f). The primary vortex ring is highly turbulent for $\ell = 315$ mm in Fig. 5 in contrast to the case for $\ell = 165$ mm in Fig. 2. The asymmetry can be attributed to peripheral motion of the multiple vortex rings in Fig. 5i–m. Like single CRVR, multiple CRVRs also move upstream and eventually interact with the trailing jet as shown in Fig. 5l–o.

3.4 Critical condition for CRVR formation

Figure 6 shows the flow visualization pictures obtained without clean flow for various M using small $\ell = 115$ mm. Here, the expansion waves catch the incident shock before they reach the shock tube exit. Hence, the velocity behind the incident shock decreases continuously and the flow is not clean (uniform). In the previous cases (Figs. 2, 3), formation of CRVR starts at $t \approx 650$ μs and its evolution is observed up to $t \approx 1,800$ μs . Therefore, the flow visualizations at different time between $t \approx 650$ and 1,800 μs are used to verify the effect of M on the formation of CRVR. The vortex ring evolution at $t = 780$ and 784 μs for $M = 1.6$ and 1.64 in Fig. 6a, b, the leading smoke front is convex. The convex profile of smoke in the leading portion ensures the weak nature of the embedded shock, which doesn't produce substantial flow deceleration at the center and therefore CRVR does not form at this Mach number. Here, the flow expansion at exit is not sufficient to induce a strong embedded shock in the axial region of the flow. Flow visualizations at $t = 770$ and 753 μs for $M = 1.67$ and 1.7 in Fig. 6c, d, respectively, the leading smoke front in the axial region is flat and shows the formation of embedded shock. However, it is not sufficiently strong to induce large velocity gradient in the annulus shear layer.

Figure 6e, f shows the vortex ring evolution at $t = 907$ and 880 μs for $M = 1.73$ and 1.77, respectively. Here, the concave leading smoke front in the axial region shows the formation of the embedded shock, which is just strong enough to create weak annulus shear layer ahead of the primary vortex ring. In Fig. 6g, a tiny CRVR is observed for $M = 1.83$ at $t = 980$ μs . This shows that the CRVR can also be generated without the clean flow. Strength of the embedded shock has to be very high for producing

substantial velocity gradient in the shear layer. The flow visualizations and inviscid calculations reveal that the M required for producing CRVR depends upon the critical strength of the embedded shock and its duration of presence. This condition is satisfied either by very high M or by long driver section length (ℓ). For any ℓ , there is a lower limit of M (1.6, Brouillette and Hebert 1997) above which the CRVR forms ahead of the primary vortex ring.

Figure 7 shows the effect of driver section length (ℓ) and Mach number (M) upon CRVR formation. Experiments are performed from $M = 1.32$ –1.9 for four driver section lengths 65, 115, 165, and 315 mm. For $\ell = 315$ mm, CRVR is observed ahead of vortex ring at $M = 1.63$. As M increases, multiple CRVR are formed, and the primary ring is severely affected by them. For $\ell = 165$ mm, CRVR forms at $M = 1.71$. Here, multiple CRVR are not observed. Strength of the CRVR increases as M increases. For $\ell = 115$ mm, CRVR that forms at $M = 1.83$ is weaker than the CRVR in higher ℓ cases. For $\ell = 65$ mm, no CRVR is formed for M up to 1.9. The dotted line in Fig. 7 shows the limit after which CRVR forms in the ℓ – M plot.

3.5 Effect of M on CRVR formation

Figure 8 shows flow visualization pictures for various M with $\ell = 315$ mm. As ℓ is large, the jet length followed by the primary ring is long and the expansion of flow continues for relatively longer time. Flow expansions eventually enhance the embedded shock strength as well as the duration of its presence in the axial region. The embedded shock causes severe stretching and deformation of primary ring seen in Fig. 8. For M up to 1.88 in Fig. 8a–d, though the primary vortex ring is seriously affected, its core structure is still preserved. At $M = 1.93$ and above, the primary vortex ring becomes highly unstable as it evolves

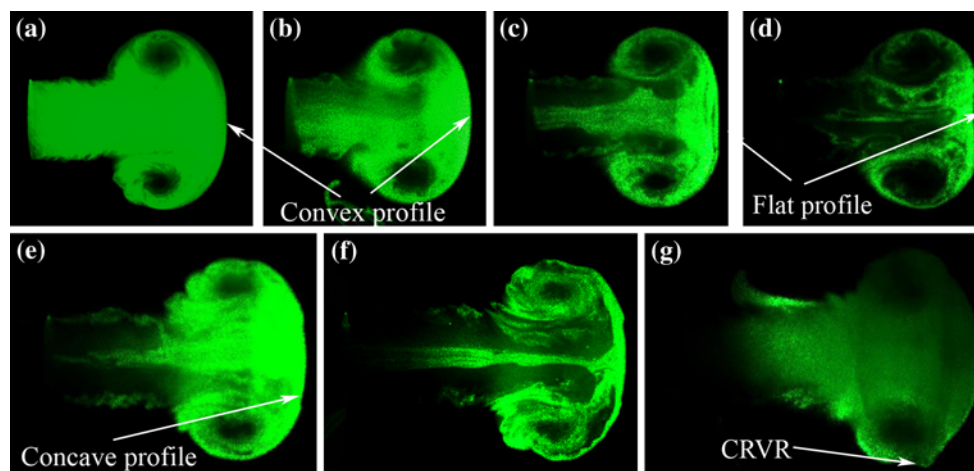


Fig. 6 Effect of M on evolution of vortex ring (a) $M = 1.6$ @ 780 μs (b) $M = 1.64$ @ 787 μs (c) $M = 1.67$ @ 770 μs (d) $M = 1.70$ @ 753 μs (e) $M = 1.73$ @ 907 μs (f) $M = 1.77$ @ 880 μs (g) $M = 1.83$ @ 980 μs for $\ell = 115$ mm

Fig. 7 Effect of driver section length and M on CRVR formation

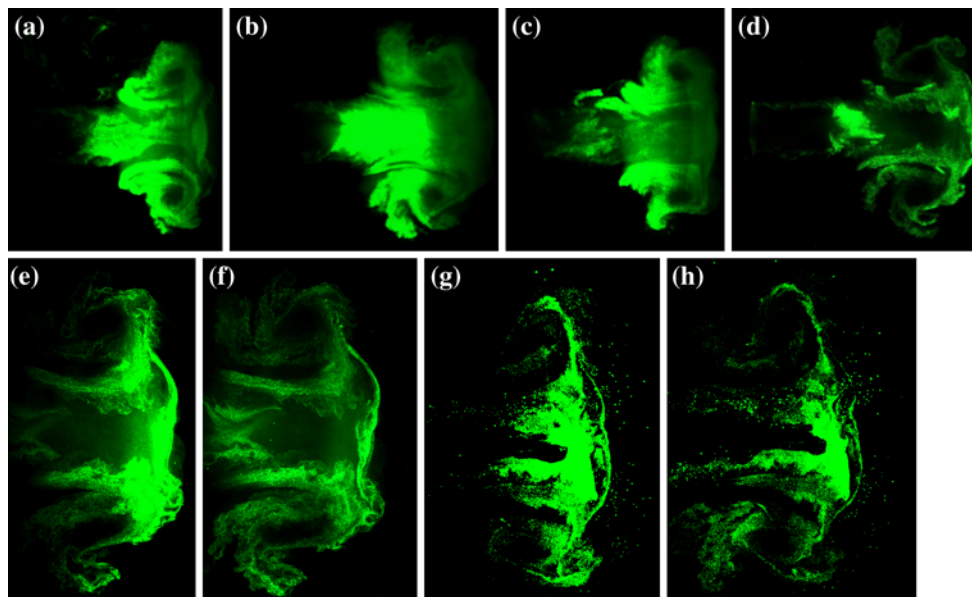
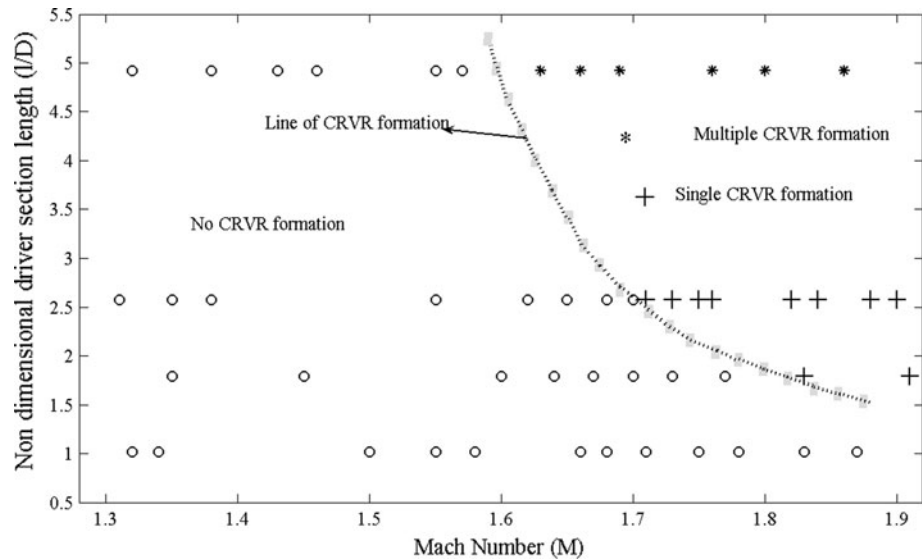


Fig. 8 Effect of M on evolution of vortex ring (a) $M = 1.84$ @ $837 \mu\text{s}$ (b) $M = 1.84$ @ $1,167 \mu\text{s}$ (c) $M = 1.88$ @ $1,073 \mu\text{s}$ (d) $M = 1.88$ @ $1,114 \mu\text{s}$ (e) $M = 1.93$ @ $1,100 \mu\text{s}$ (f) $M = 1.93$ @ $1,140 \mu\text{s}$ (g) $M = 2.1$ @ $1,020 \mu\text{s}$ (h) $M = 2.1$ @ $1,060 \mu\text{s}$ for $\ell = 315 \text{ mm}$

(Fig. 8e). For $M = 1.7$, the CRVR are stable and their identities are distinct (Fig. 5), whereas at higher $M \geq 1.93$ in Fig. 8e, f, the CRVR are difficult to identify from the primary ring. The primary vortex rings are also affected by the presence of strong CRVRs, besides the generating jet interaction for large M cases. Hence, the primary vortex ring's core also deforms and becomes an irregular turbulent structure (Fig. 8f). At $M \geq 2.1$, the smoke particles are condensed due to large expansion of flow at the exit and the flow can no longer be visualized without pre-heating the driven section gas of the shock tube.

3.6 Effect of CRVR on diameter variation

Figure 9 shows the variation of the vortex ring's diameter with non-dimensional time, $t^* (= tU_b/D)$ for $\ell = 165 \text{ mm}$ and two different M . The diameter of the vortex ring increases rapidly during initial roll up and formation for non-dimensional time, $t^* < 2$. This is attributed to significant lateral velocity of the vortex sheet during roll up at sharp exit, and flow expansion. The diameter of the vortex ring is more for large $M (=1.73)$ case compared to small $M (=1.33)$ case for same non-dimensional time, as seen in

Fig. 9 Variations of vortex ring diameter with non-dimensional time for $M = 1.33$ and 1.73 with $\ell = 165$ mm

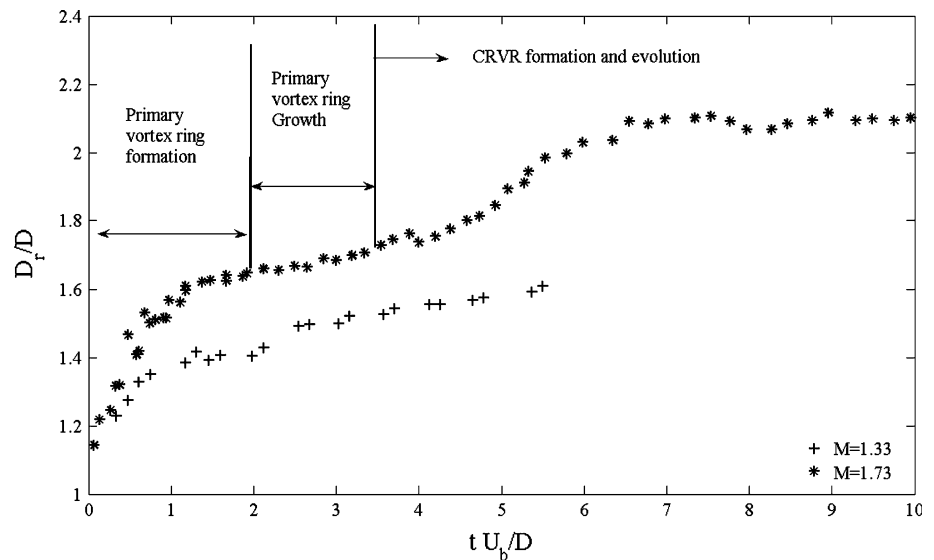


Fig. 9, is due to flow expansion. The radial growth diminishes with time, as the vortex ring translates downstream and the diameter of the vortex ring asymptotically reaches to a constant value. At $M = 1.33$, gradual increase in the diameter is observed during translation for $t^* > 3$ due to viscous diffusion. For $M = 1.7$, an embedded shock forms for $t^* > 1.3$, during the growth of the primary ring. Variation of diameter during this period is relatively slow and is the consequence of flow expansion behind and ahead of the vortex plane (Fig. 2g, C–D nozzle type flow) besides the interaction of the embedded shock with the vortex ring along the azimuthal direction. Increase in the diameter is gradual during vortex ring's evolution up to $t^* < 3.5$. However, it increases rapidly as the CRVR forms and interacts with the primary ring during its orbital motion ($3.5 < t^* < 7$). The diameter of the vortex ring reduces marginally during initiation of pinching-off at $t^* \approx 7.6$.

Figure 10 shows the variations of primary vortex ring's diameter with non-dimensional time for $\ell = 315$ mm and four different M . Here, the primary vortex ring moves larger distance with the generating jet before it pinches-off compared to the case for $\ell = 165$ mm (Fig. 9). The diameter of the vortex ring increases during formation up to $t^* < 2$ as M increases from 1.35 to 1.85. The increase in diameter at $M = 1.85$ is larger than that for $M = 1.7$. This verifies that the vortex ring diameter increases with the increase in M . Vortex rings are shock free for $M < 1.43$ (Brouillette and Hebert 1997) and vortex rings have embedded shock for $M > 1.43$. Increase in the diameter during the vortex ring's growth from $t^* \approx 2$ to 3.5 is small for $M \leq 1.45$. This shows that the expansion of the generating jet is small and the embedded shock formed in the axial region at $M = 1.45$ is very weak. This can also be inferred from Fig. 7, where a weak embedded shock is unable to produce a CRVR for $1.43 < M < 1.6$. At

$M = 1.7$ and 1.85 , the strength of the embedded shock increases (Figs. 2f–k, 8a–b) during evolution from $t^* \approx 2$ to 3.5 due to continuous expansion of the generating jet, which induces substantial lateral movement to the vortex core compared to less $M (\leq 1.45)$.

At $t^* > 3.5$, the gradual increase in diameter due to viscous diffusion is observed for $M = 1.35$ and 1.45 . For $M \geq 1.7$, the diameter of the vortex ring increases abruptly during formation of CRVR at $t^* > 3.5$. This is due to interaction of multiple CRVRs with the primary ring. Diameter of the primary vortex ring reduces considerably when CRVRs move toward the leeward side of it. Figure 11 shows the evolution of vortex ring diameter for $\ell = 165$ and 315 mm for different M . Here for $M \approx 1.3$ and 1.7 , the vortex ring diameter is large for $\ell = 315$ mm compared to the $\ell = 165$ mm. The flow expansion is larger for $\ell = 315$ mm and multiple CRVR formed ($M = 1.7$) compared to $\ell = 165$ mm. Hence, the flow expansion play major role in diameter variations. The role of CRVR in primary ring's diameter variation is discussed in Sect. 3.8.

3.7 Translational velocity of primary and CRVR

The schematic in Fig. 12a shows the position of CRVR in dotted line at various stations during its evolution along with the primary vortex core, generating jet vortices and embedded shock. Figure 12b shows the angular location, axial and lateral velocity of CRVR with respect to primary vortex ring's core for $M = 1.7$ and $\ell = 165$ mm. The angular location of the counter rotating vortex ring is measured from the primary vortex core in the clockwise direction as shown in Fig. 12a. Velocities are measured from the x and y displacement of the core in two consecutive images taken at $30 \mu\text{s}$ interval. The axial velocity is positive downstream and negative toward the shock tube

Fig. 10 Variations of vortex ring diameter with non-dimensional time for different Mach numbers for $\ell = 315$ mm

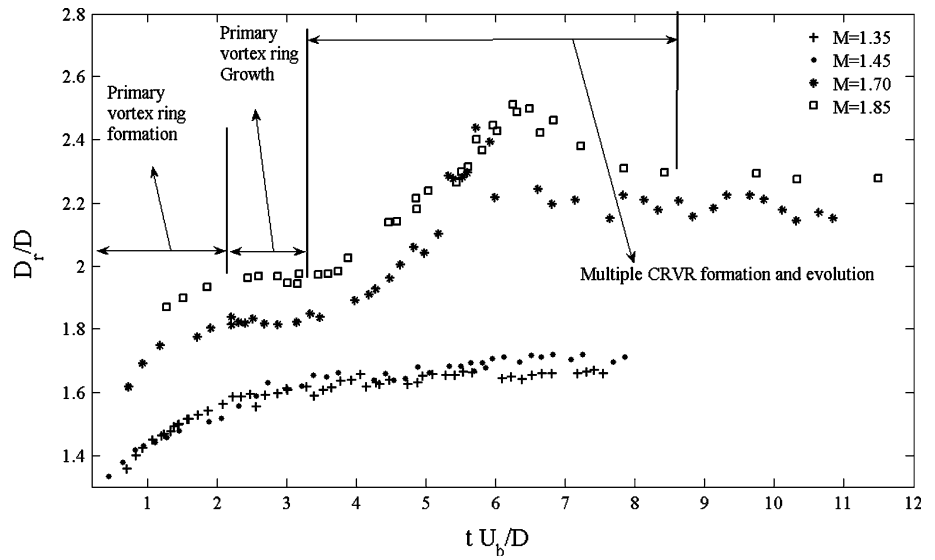


Fig. 11 Comparison of non-dimensional variations of vortex ring's diameter for $\ell = 165$ and $\ell = 315$ mm and various M

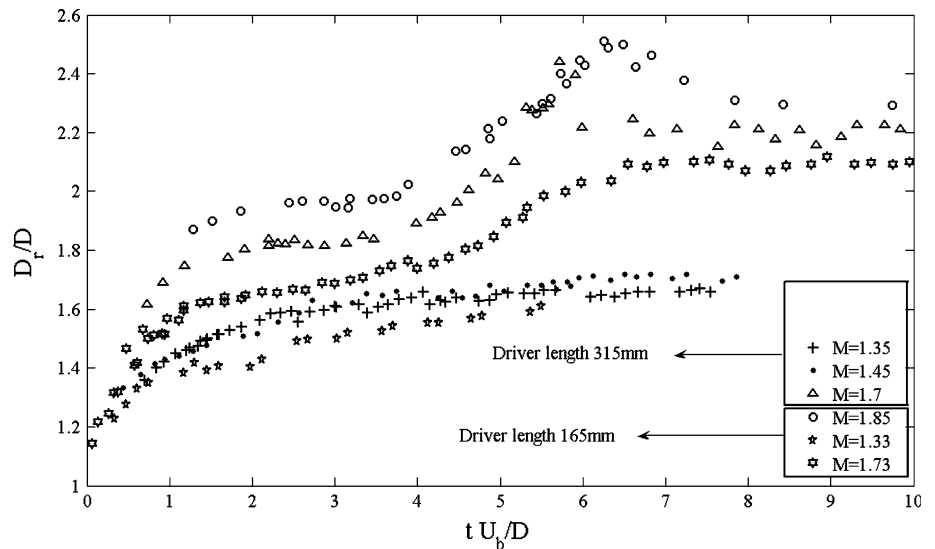
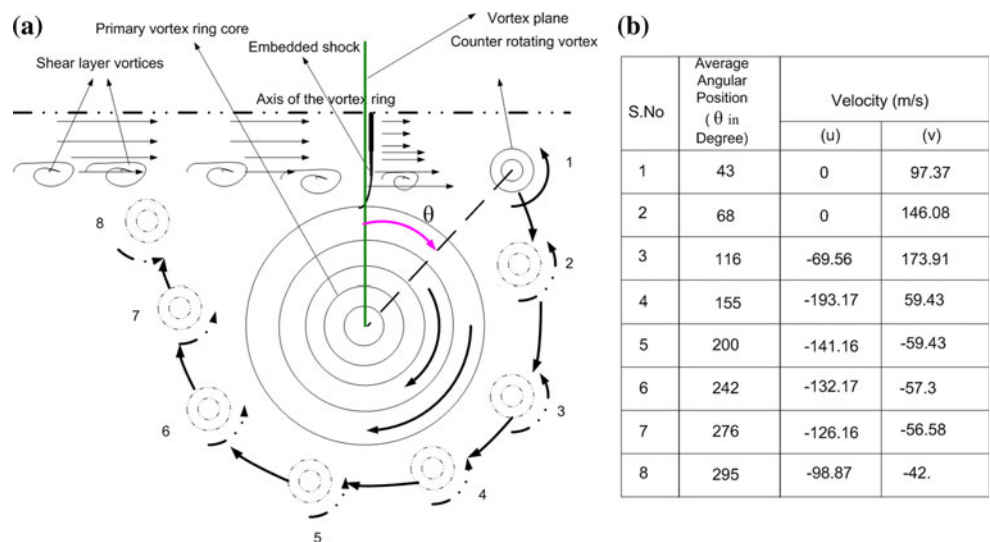


Fig. 12 a Position of CRVR along the surface of the primary ring **b** u, v velocities of CRVR in different stations for $M = 1.7$ where $\ell = 165$ mm



exit. The lateral velocity is positive in outward direction and negative toward the axis of the vortex ring. The CRVR has negligible axial velocity during its formation at stations 1 and 2. However, the lateral velocity is very high and increases continuously during its formation and growth. At station 3, CRVR has considerably negative axial velocity and it also gains additional induced velocity from the primary vortex ring due to its opposite circulation. As the axial component of induced velocity of the vortex ring is dominant at station 4, 5 and 6, the u component velocity is more compared to the v component velocity. The axial velocity reduces gradually, as CRVR moves upstream. At station 7, CRVR detaches from the primary vortex ring and its axial velocity is reduced considerably. CRVR finally interacts with the trailing jet and diffuses into a turbulent structure.

Figure 13 shows the translational velocity of the primary vortex ring and the tangential velocity of CRVR with respect to the ring, for $M = 1.7$ and $\ell = 165$ mm. The translational velocity is measured from a fixed point at the shock tube exit; hence, it is absolute. The relative tangential velocity of CRVR with respect to the vortex ring is calculated from the u and v components of velocity. For any M less than M_c , the translational velocity of the primary ring increases gradually during the formation and the growth of the primary vortex ring up to $t^* = 2$ (Arakeri et al. 2004). The translational velocity is almost constant after formation; it decreases slightly during pinching-off and moves downstream with its self-induced velocity (Arakeri et al. 2004). For M (1.7) greater than M_c , the flow at exit expands rapidly for prolonged period and the vortex ring's translational velocity continuously increases till $t^* \approx 3.2$. For $4.3 > t^* > 3.2$, the induced velocity of CRVR further increases V_r . The translational velocity decreases after $t^* \approx 4.3$ due to interaction of CRVR with

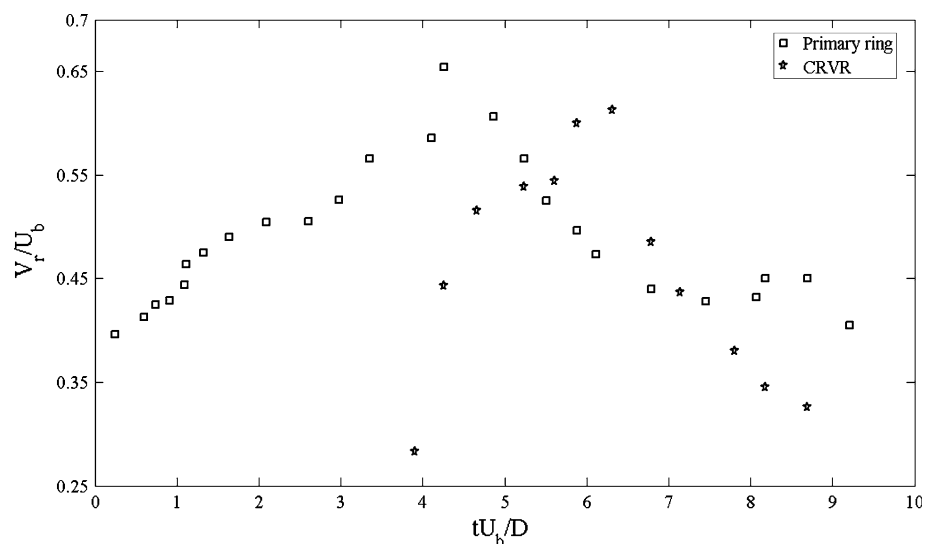
the primary ring, besides the dipping in trailing jet velocity. The effect of induced velocity is discussed in the next section.

Counter rotating vortex ring (CRVR) forms ahead of primary vortex ring at $t^* \approx 3.2$. The tangential velocity of CRVR is very small during its formation. It increases when CRVR interacts with the primary vortex ring from $t^* \approx 3.9$ to 6.4 seen in Fig. 13. The tangential velocity of CRVR is large compared to the translational velocity of ring at station 4, 5 and 6 during the orbital motion along the periphery of primary vortex ring. It reduces as CRVR reaches the rear end of the primary vortex ring. The cause of the variation of CRVR's velocity is the induced velocity of the primary ring on CRVR as explained in the next section. As the tangential velocity of CRVR reduces below the translational velocity of the primary vortex ring, it moves away from the primary vortex ring, interacts with the trailing jet and collapses into a turbulent structure.

3.8 Mechanism of diameter and translational velocity variation

Figure 14 explains the mechanism of change in diameter and velocity of the primary vortex ring during formation and evolution of CRVR. The induced velocity (U_i) of CRVR on primary vortex ring during its formation and early evolution is in outward direction in Fig. 14i, and both u and v components of induced velocity on primary ring are positive. Hence, both diameter and translational velocity of the primary vortex ring increase during CRVR formation seen in Fig. 10 and in Fig. 13 at $t^* \approx 3.6$ –4.2. The induced velocity imparted by CRVR on the primary ring is also in outward direction during its evolution in Fig. 14(ii) with positive v and negative u components of velocity. Hence, diameter increases and translational velocity

Fig. 13 Translational velocities of primary and counter rotating vortex ring for $M = 1.7$ and $\ell = 165$ mm



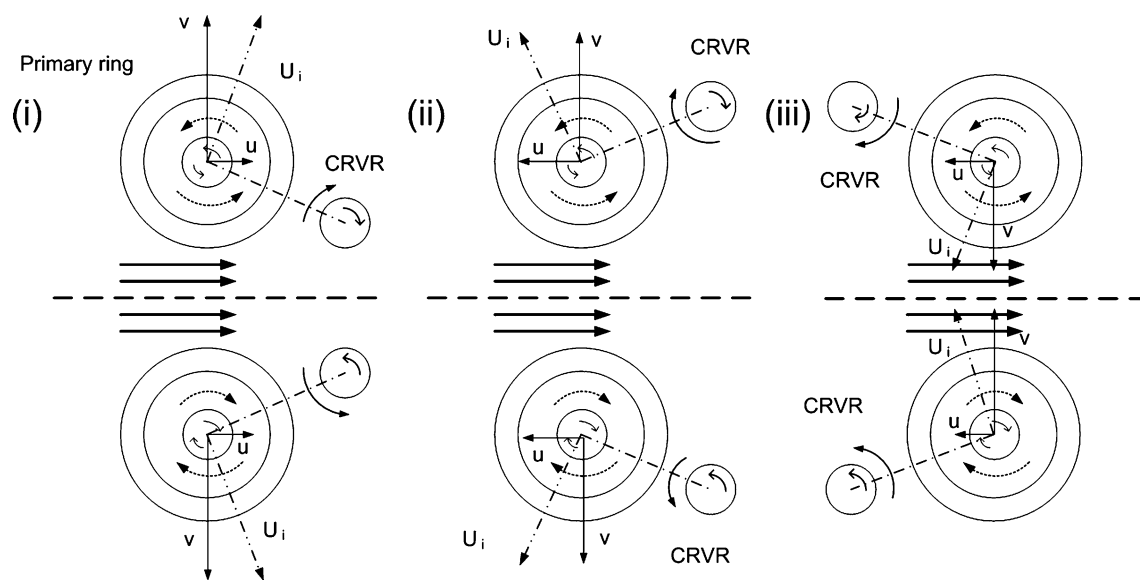


Fig. 14 Mechanism of diameter and translational velocity variations for high M vortex rings with CRVR

decreases during evolution at $t^* \approx 4.6$ in Fig. 10 and in Fig. 13. The induced velocity of CRVR on primary vortex ring is inward during later stage of CRVR's evolution in Fig. 14(iii), and both u and v components of velocities are negative. This explains why both diameter and translational velocity of primary vortex ring are reduced at later stages in Fig. 10 and in Fig. 13 for $t^* > 6.3$. Similarly, the velocity variations of CRVR can be explained in terms of the induced velocity imparted on CRVR by the primary ring. Comparison of Figs. 10, 13 indicates that the reduction in the vortex ring's velocity occurs before the reduction in diameter, which agrees with the mechanism illustrated in Fig. 14 and is a further evidence of the validity of the simple model presented.

4 Conclusion

This paper focused on formation and evolution of CRVR formed ahead of a compressible vortex ring generated at the open end of a shock tube, at High Mach number. High-speed laser sheet-based smoke flow visualizations are used to study the flow field of CRVR. At critical M , the embedded shock, being strong induces large flow deceleration along the axis of the vortex ring. In comparison, flow velocity at larger radii near the vortex core is high as the embedded shock is weak there. This results in strong velocity gradients in an annulus layer of fluid, which rolls up into CRVR ahead of primary vortex ring. Multiple CRVRs are formed as the strong embedded shock persists for prolonged period at high M and/or large ℓ cases due to Kelvin–Helmholtz type instability of the annulus shear

layer. It is also observed from flow visualization that multiple CRVRs become asymmetric due to their mutual interaction and interaction with primary ring.

The primary vortex ring is also severely disturbed during formation and evolution of CRVR. CRVRs, after formation, roll over the periphery of the primary ring either separately or merge together due to leap-frogging action. These rings move upstream and interact with the trailing jet due to entrainment. They disappear very quickly due to their opposite circulation of trailing jet vortices. Interaction of CRVRs with the jet can be of significant interest in many shock-dominated axisymmetric supersonic jets. This study also illustrates a mechanism through which the disturbances move upstream and destabilize the jet shear layers. The strength of embedded shock and the generating jet length play decisive role in formation of CRVR. The diameter of the vortex ring increases during its formation as M increases. The diameter also increases rapidly during formation of embedded shock and CRVR. The translational velocity of the primary vortex ring is also affected significantly during the formation and the evolution of CRVR. The Biot-Savart interaction of CRVR with primary vortex ring during its evolution is responsible for such variations of the vortex ring diameter and translational velocity with time.

Acknowledgments Authors acknowledge partial financial support received from Indian Space Research Organization (ISRO), India for this work. Authors are grateful to Mr. Ajay Panday and Mr. Akshaya Samal for helping in performing experiments and Dr. S. Biswas of CSJM University, Kanpur for English language corrections. Authors would like to thank the reviewers for many useful suggestions which have improved the manuscript considerably. Authors particularly

wish to acknowledge one of the reviewers who corrected us in understanding the mechanism of formation of first CRVR.

References

- Agui JH, Briassulis G, Andreopoulos Y (2005) Studies of interactions of a propagating shock wave with decaying grid turbulence: velocity and vorticity fields. *J Fluid Mech* 524:143–195
- Anderson JD (1982) *Modern compressible flow*. McGraw-Hill, New York City, pp 303–305
- Andreopoulos Y, Agui JH, Briassulis G (2000) Shock wave—turbulence interactions. *Annu Rev Fluid Mech* 32:309–345
- Arakeri JH, Das D, Krothapalli A, Lourenco L (2004) Vortex ring formation at the open end of a shock tube: a PIV study. *Phys Fluids* 16:1008–1019
- Aure R, Jacobs JW (2008) Particle image velocimetry study of the shock-induced single mode Richtmyer–Meshkov instability. *Phys Fluids* 18:161–167
- Baird JP (1987) Supersonic vortex rings. *Proc R Soc London A* 409:59–65
- Brouillette M, Hebert C (1997) Propagation and interaction of shock-generated vortices. *Fluid Dyn Res* 21:159–169
- Brouillette M, Tardif J, Gauthier E (1995) Experimental study of shock-generated vortex rings. In: Brun R, Dumitrescu LZ (eds) *Shock Waves @ Marseille*. Springer, Berlin, pp 361–366
- Cetegen BM, Hermanson JC (1995) Mixing characteristics of compressible vortex rings interacting with normal shock waves. *Combust Flame* 100:232–240
- Elder FK, Hass N (1952) Experimental study of the formation of a vortex ring at the open end of a cylindrical shock tube. *J Appl Phys* 23:1065–1069
- Gharib M, Rambod E, Shariff K (1998) A universal time scale for vortex ring formation. *J Fluid Mech* 360:121–140
- Glezer A (1988) The formation vortex rings. *Phys Fluids* 31:3532–3542
- Haertig J, Rey C, Havermann M (2006) PIV measurements of compressible vortex rings generated by a shock tube. 13th International Symposium on Application of Laser Techniques to Fluid Mechanics, Lisbon, Portugal, June 26–29, 2006
- Kontis K, An R, Edwards JA (2006) Compressible vortex-ring studies with a number of generic body configurations. *AIAA J* 44:2962–2978
- Kontis K, An R, Zare-Behtash H, Kounadis D (2008) Head-on collision of shock wave induced vortices with solid and perforated walls. *Phys Fluids* 20:016104
- Lim TT (1997) On the role of Kelvin-Helmholtz-like instability in the formation of turbulent vortex rings. *Fluid Dyn Res* 21:47–56
- Minota T (1998) Shock/vortex interaction in a flow field behind a shock wave emitted from a shock tube. *Proceedings of 2nd International Workshop on Shock Wave/Vortex Interaction*, Sendai, Japan: 149–160
- Moore DW (1985) The Effect of compressibility on the speed of propagation of a vortex ring. *Proc R Soc London A* 397:87–97
- Murugan T (2008) *Flow and Acoustic Characteristics of High Mach number Vortex Rings during Evolution and Wall-interaction: An Experimental Investigation*. Ph.D. Thesis, Department of Aerospace Engineering, Indian Institute of Technology, Kanpur
- Murugan T, Das D (2007a) Experimental investigation of acoustic characteristics of compressible vortex rings. 2nd European conference for Aerospace science 1–6 July, Brussels, Belgium
- Murugan T, Das D (2007b) Structure and acoustic characteristics of supersonic vortex ring. *FLUCOME 2007 (9th International Symposium on Fluid Control, Measurement and Visualization)* 16–21 September, Tallahassee, Florida
- Murugan T, Das D (2008) On evolution and acoustic characteristics of a compressible vortex ring. *I J Aeroacoustics* 7:199–222
- Murugan T, Das D (2009) On the evolution of counter rotating vortex ring formed ahead of a compressible vortex ring. *J Visual* 12(1):3
- Nitsche M, Krasny R (1994) Numerical study of vortex ring formation at the edge of a circular tube. *J Fluid Mech* 276:139–161
- Phan KC, Stollery JL (1983) The effect of suppressors and muzzle brakes on shock wave strength. *Proceedings of the 14th International Symposium on Shock Tubes and Waves*, Springer, Berlin, pp. 123–129
- Pullin DI (1978) The large-scale structure of unsteady self-similar rolled-up vortex sheets. *J Fluid Mech* 88:401–430
- Pullin DI (1979) Vortex ring formation at the tube and orifice opening. *Phys Fluids* 22:401–403
- Saffman PG (1978) The number of waves on unstable vortex rings. *J Fluid Mech* 84:625–639
- Thomson W (Lord Kelvin) (1871) Hydrokinetic solutions and observations. *Phil Mag* 42: 362–377
- Zare-Behtash H, Kontis K, Gongora-Orozco N (2008) Experimental investigations of compressible vortex loops. *Phys Fluids* 20:126105